

# Evidence for C, O, Al and Mg variations in the GD-1 stellar stream

Eduardo Balbinot<sup>1\*</sup>, Ivan Cabrera-Ziri<sup>2</sup>, and Carmela Lardo<sup>3</sup>

<sup>1</sup>*Kapteyn Astronomical Institute, University of Groningen, Landleven 12, NL-9747 AD Groningen, the Netherlands*

<sup>2</sup>*Astronomisches Rechen-Institut, Zentrum für Astronomie der Universität Heidelberg, Mönchhofstraße 12-14, D-69120 Heidelberg, Germany*

<sup>3</sup>*Dipartimento di Fisica e Astronomia, Università degli Studi di Bologna, Via Gobetti 93/2, 40129, Bologna, Italy*

in original form 25 November 2021

## ABSTRACT

Dynamically cold stellar streams are the relics left over from globular cluster dissolution. These relics offer a unique insight into a now fully disrupted population of ancient clusters in our Galaxy. Using a combination of Gaia eDR3 proper motions, optical and near-UV colours we select a sample of likely Red Giant Branch stars from the GD-1 stream for medium-low resolution spectroscopic follow-up. Based on radial velocity and metallicity, we are able to find 14 new members of GD-1, 5 of which are associated with the *spur* and *blob/cocoon* off-stream features. We measured C-abundances to probe for the abundance variations known to exist in globular clusters. These variations are expected to manifest in a subtle way in globular clusters with such low masses ( $\sim 10^4 M_\odot$ ) and metallicities ( $[Fe/H] \sim -2.1$  dex). We find that the C-abundances of the stars in our sample display a small but significant ( $3\sigma$  level) spread. Furthermore, we find  $\geq 4\sigma$  variations in Al- and Mg-abundances as well as a  $\sim 2\sigma$  O-abundance variation among the stars in our sample that have been observed by APOGEE. These abundance patterns match the ones found in Galactic globular clusters of similar metallicity. Our results suggest that GD-1 represents the first fully disrupted globular cluster where light-element abundance spreads have been found.

**Key words:** globular clusters: general – Galaxy: structure;

## 1 INTRODUCTION

Among the myriad of substructure present in the Milky Way (MW) halo, stellar streams stand out as being spatial and kinematic cohesive structures which in some cases span hundreds of degrees on the sky. In recent years, dozens of new streams have been discovered (e.g. Bernard et al. 2016; Balbinot et al. 2016; Malhan et al. 2018; Shipp et al. 2018; Ibata et al. 2019) and the community has exploited their properties to refine our knowledge about the mass and shape of the Galaxy as well as its accretion history (e.g. Küpper et al. 2015; Bonaca & Hogg 2018; Massari et al. 2019).

Streams are classified as *hot* or *cold*, based on the dynamical temperature (i.e. velocity dispersion) of their progenitor. The low velocity dispersion of their progenitor make *cold* stellar streams intrinsically thin ( $\lesssim 100$  pc), pointing to globular clusters (GCs) as their precursors. Palomar 5 offers a spectacular example of a *cold* stream with tidal tails radiating from a still bound cluster (e.g. Odenkirchen et al. 2001). However, in our Galaxy, *cold* streams like Palomar 5 are rare.

In fact, in the Milky Way most cold streams are progenitor-less (e.g. Shipp et al. 2018), this means that their GC progenitors are now completely dissolved. Yet, vast majority of GCs in the Galaxy

show no signs of having streams in formation (e.g. Kuzma et al. 2018; Sollima 2020).

It is natural to ask the origin of such disparity between the numbers of GC with streams and progenitor-less cold streams. It is entirely possible that the GCs that gave rise to the population of progenitor-less streams were sampled from a distribution of long gone GCs that differ from present-day MW GCs. One way of producing these fast dissolving GCs is by retaining a large fraction of stellar mass black holes, as demonstrated by Gieles et al. (2021). The authors propose two natural pathways, a low initial density or a flatter initial mass function; as well as nurture pathways, such as tidal heating and mass stripping during accretion. In this context, progenitor-less streams could be probing a population of intrinsically distinct GCs than the present-day ones in the MW. Alternatively, their progenitors may have formed in a host galaxy that is now accreted into the MW. In any of these cases, studying their remnants (stellar streams) may provide insight into population of GCs no longer available in our Galaxy.

Although historically described as simple stellar populations, in reality GC are far from it. The abundances of light elements like e.g. He, C, N, O are known change from star-to-star within a cluster (e.g. Charbonnel 2016; Gratton et al. 2019). These multiple stellar populations (MPs) seem ubiquitous in high mass GCs ( $\gtrsim 10^5 M_\odot$ ) with ages  $\gtrsim 2$  Gyr but its presence has not been established in younger low mass systems like Galactic open clusters (e.g. Car-

\* E-mail: balbinot@astro.rug.nl

ra & Martínez-Vázquez 2013; MacLean et al. 2015). The current interpretation for this is that the mechanism responsible for these abundance variations require high-mass and/or density and/or redshift to operate (see Bastian & Lardo 2018, and references therein). Unfortunately, very little is known about the presence/absence of MPs in low mass old ( $\sim 10$  Gyr) stellar clusters (Salinas & Strader 2015; Bragaglia et al. 2017). The reason for this is that such systems are very rare as their chances to get disrupted/dissolved are very high in these timescales. However, evidence for MPs in these type of systems would provide valuable insights into the mechanism responsible for their origin (which remains not very well understood). Additionally the MPs are known to be spatially segregated in many GCs (e.g. Lardo et al. 2011a; Larsen et al. 2015; Dalessandro et al. 2019) and simulations show that the two populations can remain unmixed during most of a GC lifetime (e.g. Hénault-Brunet et al. 2015). If that is the case, the outer population will escape first, leaving this spatial segregation imprinted on the distribution of stream stars. This could be exploited to pinpoint the position of the fully dissolved progenitor, ultimately leading to better dynamical models for the stream formation.

The GD-1 stream was discovered using Sloan Digital Sky Survey (SDSS; Eisenstein et al. 2011) by Grillmair & Dionatos (2006) and in recent years attracted much attention thanks to the Gaia DR2 (Gaia Collaboration et al. 2018) which allowed it to be studied in unprecedented detail (Price-Whelan & Bonaca 2018). Using collisional N-Body simulations Webb & Bovy (2019) model the dissolution process of GD-1, and conclude its progenitor must have been a very low-mass GC (a few  $10^4 M_\odot$ ), that dissolved at most in the last 3 Gyrs. Their conclusions would place the progenitor of GD-1 in the low-mass edge of the mass distribution of MW GCs and that the GD-1 progenitor would fully dissolve in a fraction of a Hubble time, possibly pointing to an extragalactic origin or atypically GC evolution/formation. The dynamical mass estimate is supported by observational constraints on the total luminous mass of GD-1 by de Boer et al. (2020), who report a mass of  $1.58 \pm 0.07 \times 10^4 M_\odot$ .

The peculiar characteristics of the GD-1 progenitor place it in a mass-age regime that is not accessible in the present population of GCs. Thus, it is interesting to investigate other properties unique to GCs. As mentioned above, some hypothesis propose that the conditions similar to the ones found in the discs of high redshift galaxies (i.e. large gas fractions, high gas densities, high turbulent speeds) enable the mechanisms responsible for producing the MPs characteristic of GCs (e.g. D’Ercole et al. 2016; Elmegreen 2017; Gieles et al. 2018; Johnson et al. 2019). The implication is that stars that form in low density environments should not host MPs.

In section 2 we present the data used to select GD-1 candidate members. In section 3 we follow-up these candidates and obtain spectra to derive radial velocities, metallicities, and abundance information. In section 4 we discuss other chemical signatures found in GD-1. And in section 5 we discuss our results and their implication.

## 2 DATA

To select GD-1 members, we use the Gaia Data Early Release 3 (eDR3; Gaia Collaboration et al. 2020), where we cross-match with LAMOST DR6<sup>1</sup> (including the subsample from Li et al. 2018),

<sup>1</sup> <http://dr6.lamost.org/v2.0/>

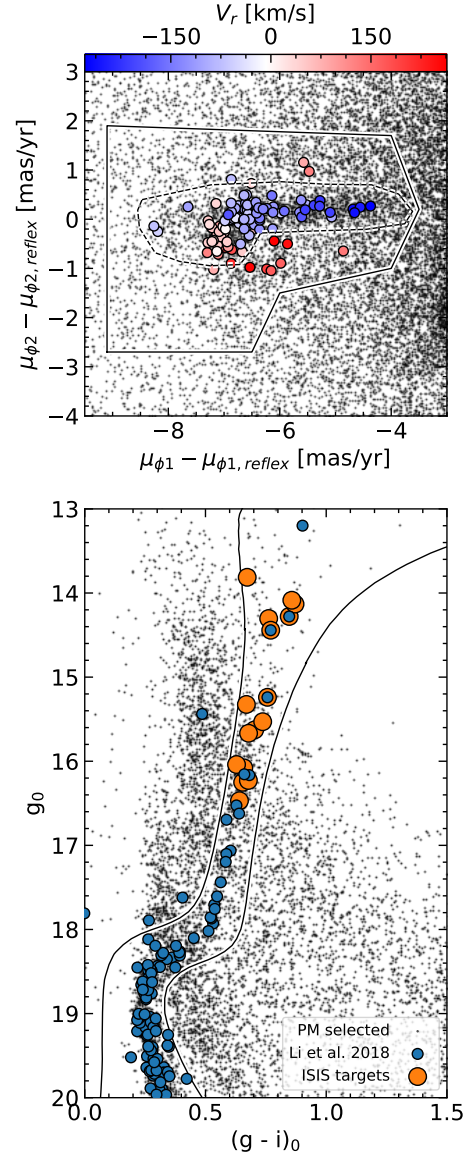


**Figure 1.** *Top panel:* PM distribution of CMD selected stars (see panel below) and with  $|\phi_2 - f(\phi_1)| < 2^\circ$ . The Li et al. (2018) sample is overlaid (blue). Colour scale shows the line-of-sight velocity. *Bottom panel:*  $(g - i)$  vs  $g$  CMD. The solid lines show a selection based on a PADOVA isochrone of  $\log_{10} \text{age/yr} = 10.03$  and  $[\text{Fe}/\text{H}] = -2.2$ . We also mark targets that were selected for spectroscopic follow-up (see Sec. 3).

SDSS DR13 photometry (Eisenstein et al. 2011), Pan-STARRS DR1 (Chambers et al. 2016), and 2MASS (Skrutskie et al. 2006).

For the astrometric catalogue of Gaia eDR3, we adopt the following quality cut:  $\text{RUWE} < 1.4$  &  $\text{visibility\_periods\_used} > 3$ . We remove some foreground stars using a parallax  $< 1$  selection. We limit our catalogue to the reported region occupied by GD-1 as reported by de Boer et al. (2018). All magnitudes in our sample were corrected for extinction using Schlegel et al. (1998) maps and Cardelli et al. (1989) extinction law, with  $R_V = 3.1$ .

The LAMOST/SDSS sample from Li et al. (2018) contains multiple observations of some stars. For these duplicates we compute the average of their line-of-sight velocities and metallicities (when available). Uncertainties were propagated accordingly.

For our analysis, it is useful to define a rotated coordinate system

( $\phi_1, \phi_2$ ) where the equator is approximately aligned with the GD-1. This system is defined via a rotation matrix given by Koposov et al. (2010). We adopt the distances from this same work to correct the proper motions (PMs) for the Solar reflex motion. The Schönrich et al. (2010) reflex motion is used, while the Sun's distance to the Galactic centre is assumed to be 8.3 kpc (Gillessen et al. 2009). We also use the best-fit 3D position of the stream to bring the stars to a common distance of 8.3 kpc, which is the stream distance at its midpoint. Throughout this paper, we use only distance normalised and de-reddened magnitudes. We also prefer Pan-STARRS magnitudes when not using the  $u$ -band.

## 2.1 Membership selection

Following a similar procedure as outlined by Price-Whelan & Bonaca (2018) we define a polygon cut in PM space. This polygon was constructed based on a sample main-sequence stars selected from a CMD cut and distance to the stream track (as defined by de Boer et al. 2018) less than  $2^\circ$  (i.e.  $|\phi_2 - f(\phi_1)| < 2^\circ$ ; where  $f(\phi_1)$  is the interpolated stream track). In order to define a more robust colour-magnitude selection, that includes Red Giant Branch (RGB) stars, we use the PM selected sample and the spectroscopically confirmed sample to define a narrow colour-magnitude cut. When compared to the PM selection from Price-Whelan & Bonaca (2018), our selection is more restrictive, mainly due to RGB stars being brighter, thus having lower astrometric uncertainties. We also note that some spectroscopically confirmed members are not included in our PM selection, these members are typically close to the lower limit in  $\phi_1$ , which was not favoured in our selection due to observability constraints (see Sec. 3).

In Figure 1 we show a summary of our selection process. In the top panel the PM selection polygon is shown, while the sample from Li et al. (2018) is over-plotted. The colour-scale indicate the radial velocity value. On the bottom panel, the colour-magnitude diagram (CMD) for the PM-selected sample is shown. To define a CMD selection around likely GD-1 members we use a PARSEC isochrone (Bressan et al. 2012). Our best-fit isochrone is defined as the one that well represents the main-sequence, and is able to reproduce the observed RGB members from Li et al. (2018). It is out of the scope of this paper to produce a robust isochrone fit, we are interested only in defining a region of the CMD that contains likely GD-1 member stars. A range of colours around the best-fit isochrone is defined based on the photometric uncertainties, while allowing for a wider range in colours at bright magnitudes in order to include regions of the CMD where confirmed GD-1 members occupy. In the same Figure we also define a new PM selection based on the spectroscopic members, as discussed above.

In the literature, combinations of filters have often been used to pick up the variations in specific spectral features characteristic of the MPs phenomena (e.g. Marino et al. 2008; Lardo et al. 2011b; Monelli et al. 2013). Here we exploit the  $C_{ugi}$  colour index, which is sensitive to CN molecular bands around 385 nm originating from cold stellar atmospheres. This index is defined as:

$$C_{ugi} = (u - g) - (g - i) \quad (1)$$

$$\sigma_{ugi} = \sqrt{\sigma_u^2 + 2\sigma_g^2 + \sigma_i^2} \quad (2)$$

where  $\sigma_{ugi}$  is the photometric uncertainty propagated from the uncertainties in  $u$ ,  $g$  and  $i$ .

Besides being an indicator for MPs, this colour index is also highly sensitive to metallicity. In Figure 2 we show the  $C_{ugi}$  CMD

for stars selected based on PM (narrow selection) and optical CMD (see Figure 1). We show the CMD for an *on-stream* regions (top left panel), defined as  $|\phi_2 - f(\phi_1)| < 2^\circ$ , and an *off-stream* region (top right panel), defined as  $|\phi_2 - f(\phi_1) - 4^\circ| < 2^\circ$ . The *off-stream* shows the CMD locus occupied by MW field stars that comply with both our PM and CMD cuts. Based on the best-fit isochrone, we define a region where contaminants are likely to be found (highlighted in yellow). Notice that due to the uncertainty of the isochrone fit, we allow for a broader range in colour at brighter magnitudes. To confirm that these stars are contaminants we show their radial velocity distribution as a function of  $\phi_1$  (i.e. along the stream). When compared to the best-fit orbit from Koposov et al. (2010) (dashed line) we see that many of the stars have velocities incompatible with the stream. A few stars overlap with the expected velocity trend, but on closer inspection, their metallicity is inconsistent with the bulk of the GD-1 stars (bottom right panel). We find that the  $C_{ugi}$  selection is able to remove most of the contaminants, and the few ones left either have incompatible velocities and/or metallicities. We also note the existence of a few LAMOST DR6 stars that could be GD-1 members and that are not in the Li et al. (2018) sample. We follow-up these potential members in the more recent LAMOST DR7 and find that several of these stars have multiple epoch observations. We compute their averaged spectra, metallicities, and velocities from the LAMOST database. We select GD-1 members with radial velocities consistent ( $< 3\sigma_{V_{los}}$ ) with the stream orbit and  $[\text{Fe}/\text{H}] < -1.75$ . We use this data in conjunction with the newly obtained spectra presented in the following section.

## 3 SPECTROSCOPIC FOLLOW-UP

Using the bright high-probability RGB sample defined above we obtained spectra using the Intermediate-dispersion Spectrograph and Imaging System (ISIS) at the 4.2m William Herschel Telescope (WHT; program SW2019a05). We use the R300B configuration for the blue-arm, yielding a  $R \sim 300$  in the wavelength range of [325, 520] nm. The red-arm was setup in the R1200R mode, yielding a  $R \sim 5000$  in the Calcium Triplet spectral region ([830, 890] nm). The exposure time was adjusted such as to yield a S/N of at least 10 at 338nm in the blue-arm.

We targeted 23 stars based on the membership selection outlined in Section 2.1, these were observed in the course of two nights in December 2019. Standard long-slit reduction was performed using IRAF, wavelength calibration was done using CuThAr arc-exposures taken at after each exposure and at the end and beginning of the night. We note that at the time of the observations, only Gaia DR2 data was available, and 23 targets were selected for observation, out of which only the 16 higher priority stars were observed due to scheduling and weather. Coincidentally the stars that were not observed turned out to not pass our selection criteria with the updated Gaia eDR3 data. For completeness and compatibility with the observing proposal data, we chose to keep the star ids running from 1 to 23, even though only 16 stars were observed.

We derived the effective temperature and gravity for the stars in our sample with the code BRUTUS<sup>2</sup> (Speagle et al. 2021), using as input the Pan-STARRS and 2MASS photometry and a prior on the distance coming from the stream track (with 0.5 kpc uncertainties). These values are reported in Table 1.

As sanity check, we also use the our spectra to get independent

<sup>2</sup> <https://github.com/joshspeagle/brutus>

**Table 1.** IDs, eDR3 `source_id`, rotated coordinates, G-magnitude, blue-arm atmospheric parameters; red-arm radial velocities and metallicity measurements of our targets. Stars in common with Li et al. (2018) and APOGEE DR16 (Ahumada et al. 2020) have their `source_id` marked with an \* and †, respectively. We also list the effective temperature ( $T_{\text{eff,phot}}$ ) and surface gravity ( $\log g_{\text{phot}}$ ) derived from photometry (see Sec. 3). For LAMOST DR7 stars, we list the metallicity and velocity measured by their pipeline, taking their average when multi-epoch data is available.

ID	source_id	$\phi_1$ deg	$\phi_2$ deg	G mag	$T_{\text{eff,blue}}$ K	$\log g_{\text{blue}}$ dex	$T_{\text{eff,phot}}$ K	$\log g_{\text{phot}}$ dex	$V_{\text{los}}$ km/s	[Fe/H] dex
ISIS Members										
4	686849456285987840†	-56.31766	0.15197	15.43	5240 <sup>+52</sup> <sub>-65</sub>	2.35 <sup>+0.15</sup> <sub>-0.29</sub>	5365 ± 38	2.71 ± 0.04	98.39 <sup>+3.04</sup> <sub>-3.21</sub>	-2.10 <sup>+0.32</sup> <sub>-0.37</sub>
6	696138061798355840	-48.90048	-0.26598	14.55	5138 <sup>+15</sup> <sub>-77</sub>	1.82 <sup>+0.07</sup> <sub>-0.65</sub>	5181 ± 41	2.32 ± 0.05	49.87 <sup>+0.90</sup> <sub>-1.08</sub>	-2.03 <sup>+0.05</sup> <sub>-0.07</sub>
8	796283127046157312	-40.40242	0.71651	15.29	5355 <sup>+38</sup> <sub>-61</sub>	2.43 <sup>+0.12</sup> <sub>-0.26</sub>	5299 ± 79	2.65 ± 0.06	-13.31 <sup>+2.86</sup> <sub>-2.26</sub>	-2.31 <sup>+0.33</sup> <sub>-0.43</sub>
9	796217426927895168*†	-40.28003	0.13156	13.42	5299 <sup>+5</sup> <sub>-5</sub>	2.00 <sup>+0.03</sup> <sub>-0.01</sub>	4918 ± 12	1.86 ± 0.06	-11.75 <sup>+0.54</sup> <sub>-0.61</sub>	-2.00 <sup>+0.02</sup> <sub>-0.01</sub>
10	796779998924250624	-38.45281	0.17051	15.56	5255 <sup>+58</sup> <sub>-68</sub>	2.03 <sup>+0.30</sup> <sub>-0.36</sub>	5395 ± 46	2.80 ± 0.05	-23.28 <sup>+3.02</sup> <sub>-3.02</sub>	-2.24 <sup>+0.48</sup> <sub>-0.46</sub>
12	805475834527735168*	-32.92161	1.13310	13.26	5036 <sup>+6</sup> <sub>-3</sub>	1.00 <sup>+0.25</sup> <sub>-0.05</sub>	4838 ± 58	1.64 ± 0.05	-64.71 <sup>+1.08</sup> <sub>-0.83</sub>	-1.97 <sup>+0.10</sup> <sub>-0.05</sub>
13	832080270707721088*	-25.31829	0.25339	14.45	5051 <sup>+73</sup> <sub>-3</sub>	1.03 <sup>+0.90</sup> <sub>-0.93</sub>	5123 ± 62	2.18 ± 0.05	-114.73 <sup>+0.99</sup> <sub>-1.22</sub>	-2.01 <sup>+0.03</sup> <sub>-0.05</sub>
16	840073411003209216	-15.37631	-1.02189	15.13	5164 <sup>+62</sup> <sub>-101</sub>	1.62 <sup>+0.27</sup> <sub>-0.63</sub>	5216 ± 46	2.44 ± 0.06	-175.37 <sup>+2.30</sup> <sub>-1.53</sub>	-2.06 <sup>+0.13</sup> <sub>-0.18</sub>
17	790916754387404928	-15.85484	-2.62079	14.78	5370 <sup>+35</sup> <sub>-43</sub>	2.50 <sup>+0.19</sup> <sub>-0.19</sub>	5479 ± 56	2.24 ± 0.06	-169.52 <sup>+2.12</sup> <sub>-2.16</sub>	-2.19 <sup>+0.21</sup> <sub>-0.39</sub>
18	840818192691653504	-12.87469	-0.09236	15.61	5200 <sup>+57</sup> <sub>-36</sub>	1.74 <sup>+0.16</sup> <sub>-0.17</sub>	5377 ± 31	2.62 ± 0.06	-190.59 <sup>+2.74</sup> <sub>-2.26</sub>	-2.17 <sup>+0.28</sup> <sub>-0.43</sub>
19	840727860939569152	-12.50469	-0.23993	15.14	5252 <sup>+47</sup> <sub>-54</sub>	2.35 <sup>+0.18</sup> <sub>-0.30</sub>	5291 ± 25	2.42 ± 0.05	-189.35 <sup>+2.75</sup> <sub>-2.07</sub>	-2.22 <sup>+0.25</sup> <sub>-0.50</sub>
20	1573344450075107456	-10.91051	-0.73733	15.65	5394 <sup>+35</sup> <sub>-44</sub>	2.50 <sup>+0.16</sup> <sub>-0.22</sub>	5382 ± 31	2.65 ± 0.05	-201.09 <sup>+2.75</sup> <sub>-2.89</sub>	-2.36 <sup>+0.40</sup> <sub>-0.49</sub>
23	1576400508285430272	-4.18422	-2.58857	13.72	5038 <sup>+109</sup> <sub>-3</sub>	1.02 <sup>+0.97</sup> <sub>-0.02</sub>	5000 ± 45	1.67 ± 0.05	-233.72 <sup>+0.80</sup> <sub>-0.69</sub>	-1.99 <sup>+0.05</sup> <sub>-0.04</sub>
ISIS Non-members										
1	684655586991056512	-59.94303	1.28547	12.84	5062 <sup>+2</sup> <sub>-2</sub>	2.99 <sup>+0.01</sup> <sub>-0.02</sub>	4890 ± 55	1.52 ± 0.06	49.77 <sup>+0.50</sup> <sub>-0.45</sub>	-1.20 <sup>+0.09</sup> <sub>-0.09</sub>
2	685227642275283456	-57.91505	0.80182	13.39	5064 <sup>+3</sup> <sub>-3</sub>	2.89 <sup>+0.04</sup> <sub>-0.03</sub>	4825 ± 25	1.76 ± 0.06	94.09 <sup>+0.68</sup> <sub>-0.65</sub>	-1.35 <sup>+0.11</sup> <sub>-0.20</sub>
11	747560017309217792	-39.49137	-1.97128	13.07	5040 <sup>+3</sup> <sub>-5</sub>	2.64 <sup>+0.03</sup> <sub>-0.04</sub>	4857 ± 40	1.62 ± 0.06	-4.39 <sup>+0.60</sup> <sub>-0.61</sub>	-1.53 <sup>+0.08</sup> <sub>-0.08</sub>
LAMOST DR7										
-	793009399891751040	-45.78102	0.08422	15.92	-	-	5487 ± 36	2.97 ± 0.04	23.45 ± 8.56	-2.19 ± 0.10
-	793910484031755264*	-44.65316	0.09744	15.62	-	-	5388 ± 60	2.82 ± 0.04	15.11 ± 7.85	-2.23 ± 0.10
-	802849960243599872	-37.86740	0.43362	15.88	-	-	5490 ± 37	2.93 ± 0.05	-27.40 ± 7.14	-2.21 ± 0.10
-	829645264771612800	-27.34517	0.17882	15.99	-	-	5316 ± 50	2.89 ± 0.06	-102.87 ± 6.36	-1.79 ± 0.05
-	832022718144536192*	-22.00954	-0.03175	15.97	-	-	5346 ± 62	2.85 ± 0.06	-142.68 ± 6.86	-2.08 ± 0.13
-	1573762367572774272	-10.41675	-0.24961	15.74	-	-	5002 ± 46	1.67 ± 0.05	-207.65 ± 4.63	-2.30 ± 0.03

estimates for the temperatures and gravities of these stars. For this we analysed the one-dimensional reduced and calibrated spectra using `rvspecfit` (Koposov et al. 2010) with PHOENIX v2.0 spectral library (Husser et al. 2013). To obtain reliable uncertainties, we use a Markov-Chain Monte Carlo (MCMC) minimisation that allows for  $T_{\text{eff}}$ ,  $\log g$ , radial velocity, and metallicity to be free. We estimated the best-fit values as the median of the posterior chains, while taking the 25 and 75 percentiles as their respective uncertainties. We found that the red-arm spectra had little constraining power over  $\log g$ , and often would converge to the edge of our model grid. Thus we chose to report the values for  $T_{\text{eff}}$  and  $\log g$  coming from the blue-arm (see Table 1). We found overall a good agreement between the spectroscopic and photometric stellar parameters. We note that the overall results and conclusions presented below are not dependent on the choice between spectroscopic and photometric  $T_{\text{eff}}$  and  $\log g$ .

Although the fitting process described above was applied to spectra from both ISIS arms, we chose to use the red-arm for the velocity and metallicity, since it is higher resolution and allows for a comparison with CaT metallicity determinations. These values can also be found in Table 1. In Figure 3 we show the method used to select members based on the inferred radial velocity and metallicities. We find that for the 16 Gaia eDR3 selected stars observed 13 are likely members based on a  $[\text{Fe}/\text{H}] < -1.75$  selection alone, and find a weighted average metallicity of  $-2.06 \pm 0.10$  for this metallicity selected sample. We compare our metallicities to those derived using the CaT equivalent width (Vázquez et al. 2015) and find them to agree within 0.1 dex. When comparing the offset in radial velocity with GD-1 best-fit orbit, we observe that all low-metallicity stars fall within  $2\sigma$  ( $\sim 7.5 \text{ km s}^{-1}$ ) of the mean, with the out-

liers (marked as non-members) being the three highest metallicity stars. We thus conclude that a metallicity selection is sufficient to weed out contaminants in our ISIS sample, as it has already been demonstrated Figure 2. The LAMOST DR7 sample was originally constructed using our narrow PM+CMD selection and with added radial velocities, we find that this selection is enough to weed out most contaminants. A single high-metallicity star was identified in this sample and removed from the analysis. We note that the range in  $\phi_1$  where the three ISIS non-members are located is also where GD-1's orbital line of sight velocity is the most similar to field stars.

In Figure 4 we show the spatial distribution high-probability RGB members. Confirmed RGB members from Li et al. (2018) are shown, as well as all the stars where ISIS or LAMOST DR7 spectra is available, however only the former has labels corresponding to their ID (see Tab. 1). We limit the spectroscopic samples to the magnitude range of the RGB. We also allow for a fainter selection (black dots) which illustrates the location of the bulk of GD-1's stars.

We find two members in the *spur* region, star #12 which is reported by Li et al. (2018), and #8 closer to the main stream track. We also find stars #16, #17, and #23 to be in the region associated the (blob/cocoon; Price-Whelan & Bonaca 2018; Malhan et al. 2018). Stars #17, and #23 are the most track deviant GD-1 confirmed member ever detected. We note that very few RGB candidates remain to be followed up in the main body of GD-1, possibly indicating that most RGB belonging to this stream have been found already.



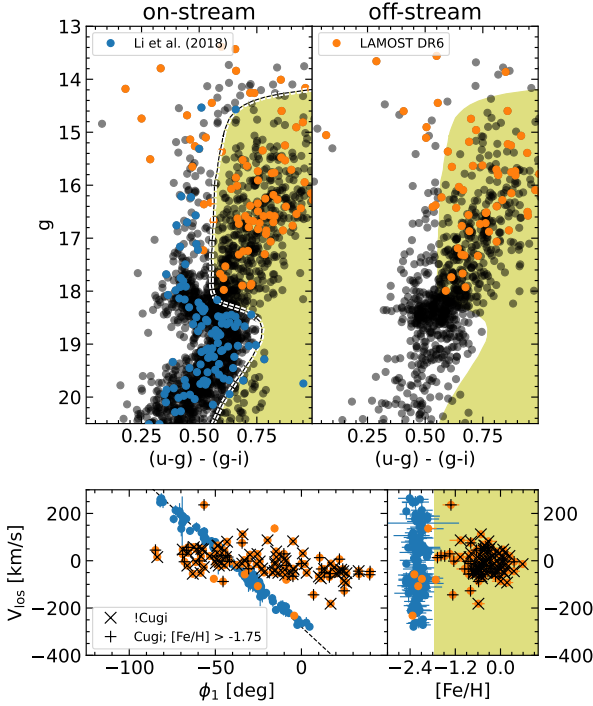


**Figure 2.** *Top left:*  $C_{u gi}$  CMD of the narrow-PM and optical-CMD selected sample. We highlight the Li et al. (2018) (blue) and LAMOST DR6 samples (orange). We overlay the same isochrone used in Figure 1, shifted in colour (dashed line) to define a selection of potential members. The yellow shaded region marks the CMD region likely to contain only field stars. *Top right:* same as previous panel, but for *off-stream* stars ( $|\phi_2 - f(\phi_1) - 4^\circ| < 2^\circ$ ). *Bottom left:*  $v_r$  as a function of  $\phi_1$ , the dashed line is the best-fit orbit from Koposov et al. (2010). We overplot  $\times$  on stars that are likely to be contaminant from their position in the  $C_{u gi}$  CMD. Stars marked with  $+$  signs are removed from the sample since their LAMOST DR6 metallicities do not comply with the bulk of GD-1 stars (*bottom right panel*).

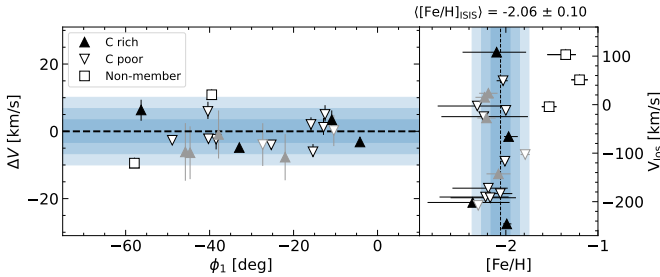


**Figure 3.** ISIS red-arm radial velocity vs  $\phi_1$  (*left*) and metallicity (*right*). Members are marked with up/down triangles depending on their measured C-abundance (see Section 3.1), non-members are shown as squares. On the *left* the velocities have been subtracted by the best-fit Koposov et al. (2010) orbit. Both panels show the mean (dashed line) as regions 1, 2, and 3  $\sigma$  away from it (shaded blue tones), computed using a uncertainty-weighted average. We note that one of the high-metallicity non-members lie outside of the velocity range in the *left panel*. In both panels we show LAMOST DR7 stars in grey, following the same notation as before. These were not used to compute the confidence intervals and average metallicity.

**Table 2.** Measured CH and CN indices, derived carbon abundances and corrections (Placco et al. 2014).

ID	CN	CH	A(C)	$\Delta A(C)_{corr}$
-	mag	mag	dex	dex
ISIS				
4	$-0.13 \pm 0.03$	$-0.42 \pm 0.04$	$6.67 \pm 0.09$	0.01
6	$-0.19 \pm 0.02$	$-0.43 \pm 0.03$	$6.52 \pm 0.08$	0.01
8	$-0.19 \pm 0.02$	$-0.45 \pm 0.04$	$6.42 \pm 0.13$	0.01
9	$-0.17 \pm 0.02$	$-0.47 \pm 0.02$	$5.39 \pm 0.07$	0.13
10	$-0.20 \pm 0.02$	$-0.43 \pm 0.03$	$6.69 \pm 0.11$	0.01
12	$-0.16 \pm 0.02$	$-0.41 \pm 0.02$	$6.09 \pm 0.11$	0.40
13	$-0.18 \pm 0.02$	$-0.38 \pm 0.03$	$6.47 \pm 0.10$	0.01
16	$-0.18 \pm 0.02$	$-0.42 \pm 0.03$	$6.43 \pm 0.08$	0.01
17	$-0.18 \pm 0.02$	$-0.43 \pm 0.03$	$6.76 \pm 0.12$	0.01
18	$-0.19 \pm 0.03$	$-0.44 \pm 0.04$	$6.74 \pm 0.09$	0.01
19	$-0.19 \pm 0.04$	$-0.42 \pm 0.04$	$6.64 \pm 0.09$	0.01
20	$-0.16 \pm 0.03$	$-0.45 \pm 0.04$	$6.50 \pm 0.06$	0.01
23	$-0.16 \pm 0.02$	$-0.40 \pm 0.03$	$6.39 \pm 0.08$	0.33
LAMOST DR7				
696138 <sup>a</sup>	$-0.03 \pm 0.10$	$-0.40 \pm 0.07$	$6.62 \pm 0.13$	0.01
793009	$-0.13 \pm 0.06$	$-0.45 \pm 0.03$	$6.91 \pm 0.13$	0.01
793910	$-0.12 \pm 0.04$	$-0.44 \pm 0.04$	$6.73 \pm 0.15$	0.01
802849	$-0.15 \pm 0.05$	$-0.44 \pm 0.05$	$6.76 \pm 0.13$	0.01
829645	$-0.15 \pm 0.04$	$-0.46 \pm 0.03$	$6.65 \pm 0.19$	0.01
832022	$-0.20 \pm 0.06$	$-0.34 \pm 0.04$	$7.14 \pm 0.16$	0.01
832080 <sup>b</sup>	$-0.12 \pm 0.04$	$-0.44 \pm 0.02$	$6.46 \pm 0.14$	0.01
157376	$-0.12 \pm 0.04$	$-0.43 \pm 0.02$	$6.57 \pm 0.15$	0.01
157640 <sup>c</sup>	$-0.10 \pm 0.03$	$-0.42 \pm 0.03$	$6.43 \pm 0.14$	0.33

<sup>a</sup> star no. 6 in the ISIS sample, <sup>b</sup> star no. 13 in the ISIS sample, <sup>c</sup> star no. 23 in the ISIS sample.

### 3.1 CN, CH and Carbon abundances

We have calculated the band strengths  $S\lambda 3883$  (CN) and  $CH\lambda 4300$  (CH) to investigate the presence of multiple populations in GD-1. This technique has been extensively used for GCs in the Galaxy (e.g. Kayser et al. 2008; Martell & Smith 2009; Pancino et al. 2010; Lardo et al. 2013) and clusters in its dwarf satellites (e.g. Hollyhead et al. 2017, 2018, 2019; Martocchia et al. 2021). Indices sensitive to absorption by the 4300Å CH and the 3883Å CN bands were measured as described in Norris & Freeman (1979) and Norris et al. (1981)<sup>3</sup>. Errors on measurements are calculated assuming Poisson statistics, following Vollmann & Eversberg (2006).

In the left-hand panels of Figure 5, we show the strength of the  $S\lambda 3883$  (CN) and  $CH\lambda 4300$  (CH) indices as a function of the surface gravity ( $\log(g)$ ) of each star in the ISIS and LAMOST sample (black and grey symbols, respectively). To account for any trend of the indices with atmospheric parameters we fit a linear model by robust regression –which attempts to down-weight the influence of outliers in order to provide a better fit to the majority of the data (e.g., Venables & Ripley 2002) – between index measurements and  $\log(g)$ . This has been done for the ISIS and LAMOST data-sets separately to properly take into account possible offsets between the two data sources sets before analysing and interpreting results. Indeed, while for the  $CH\lambda 4300$  index data from ISIS and LAMOST spectra are on the same scale (see bottom left-hand panel of Figure 5), this is not

<sup>3</sup> The blue-arm ISIS spectra extends to wavelengths where in principle the NH indices could be measured, however the spectra is of too low S/N at those wavelengths.

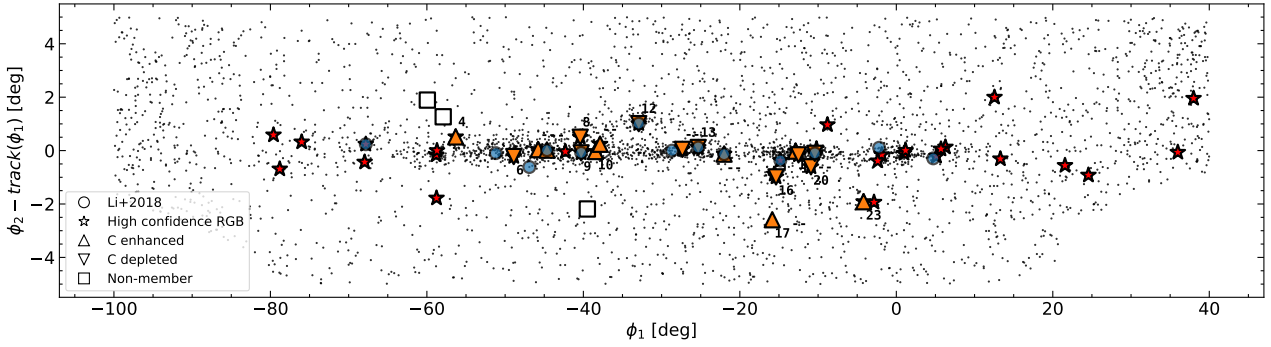


**Figure 4.** Spatial distributions of CMD (optical and near UV) and PM (narrow) selected stars (black). High probability RGB stars in the magnitude range of  $14 < g < 17$  are shown as red stars. We split our spectroscopic sample into three groups, C rich/poor (see Section 3.1), and non-members (see Figure 3). Stars in our ISIS spectroscopic sample are labelled by their ID (see Table 1). The Li et al. (2018) sample is shown as blue circles.

the case for the CN index. The top left-hand panel of Figure 5 shows that the  $y$ -intercept of the best fit linear model ( $b_0$ ) is clearly different for the two samples ( $b_0 = -0.117 \pm 0.013$  and  $-0.033 \pm 0.044$  for ISIS and LAMOST, respectively), whereas its slope is virtually identical. This is likely because the “one-sided” CN index is more sensitive to factors such as e.g. spectral resolution and quality of the flux calibration than the “two-sided” CH index. Differences between the measured  $S\lambda 3883$  (CN) index from the ISIS and LAMOST spectra are of the order of the  $\Delta S\lambda 3883$  (CN)<sub>(ISIS-LAMOST)</sub> =  $-0.65$  mag for both ISIS stars #13 and #23 (stars 832080 and 157640 in LAMOST, respectively), which is comparable to the observed zero-point between the two data-sets. A larger difference is observed for ISIS star #6 (star 696138 in LAMOST). However the index measurements for this star are also characterised by very large errors, so the observed discrepancy is likely due to the lower quality of the LAMOST spectrum.

Indices corrected for temperature and gravity effects (denoted as  $\delta\text{CN}$  and  $\delta\text{CH}$ ) have been obtained by subtracting the robust linear models shown in Figure 5 from the computed  $S\lambda 3883$  (CN) and  $\text{CH}\lambda 4300$  indices. Their distribution is plotted in the right-hand panels of Figure 5. In the same panels the  $\delta\text{CN}$  kernel density distribution is also shown along with the best fit Gaussian<sup>4</sup>. No evidence for intrinsic  $\delta\text{CN}$  and  $\delta\text{CH}$  variations that exceed measurement errors can be derived from a careful inspection of the right-hand panels of Figure 5.

We further investigate the presence of any spreads by modelling the distribution in  $\delta\text{CN}$ , and  $\delta\text{CH}$  as a 1D normal distribution to our data. Here we assume that for each data point a total dispersion can be computed in the form of  $\sigma^2 = \sigma_0^2 + \sigma_j^2$ , i.e. the sum in quadrature of an intrinsic dispersion and the uncertainty in each  $j$ -th data point. We fit this distributions to compute a likelihood that is maximized using *emcee* (Foreman-Mackey et al. 2013). We find an intrinsic dispersion of  $\sigma_{0,\text{CH}} = 0.011 \pm 0.008$  for  $\delta\text{CH}$ ; and  $\sigma_{0,\text{CN}} = 0.008 \pm 0.007$  for  $\delta\text{CN}$ . Both these dispersions are consistent with zero at the a  $3\text{-}\sigma$  level. Thus, it is not possible to reveal any sign of CN or CH intrinsic variations among GD1 stars from low-resolution spectra.

Although our ISIS spectra does not have the SNR to provide a reliable nitrogen abundance, it was good enough to derive carbon abundances. These were inferred by fitting observed spectra with

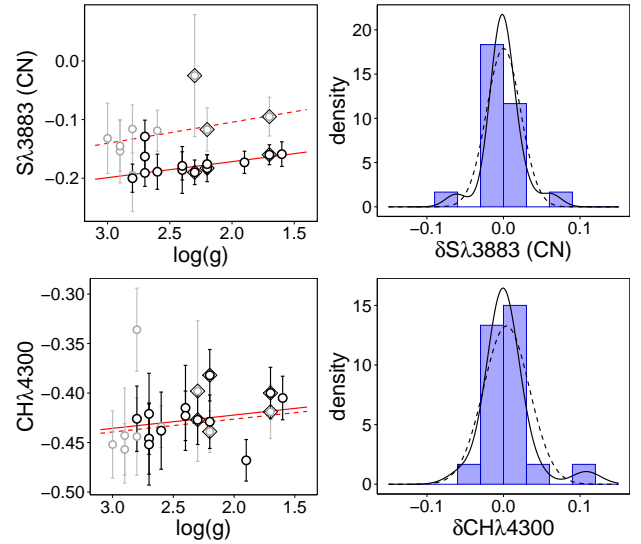


**Figure 5.** The left-hand panels shows the run of the  $S\lambda 3883$ (CN) (top) and  $\text{CH}\lambda 4300$  (bottom) indices against the surface gravity ( $\log(g)$ ) for GD1 member stars. Stars from the ISIS and LAMOST data-sets are plotted in black and grey colour, respectively. The solid and dashed red lines indicate the linear fit of those quantities versus magnitude for the ISIS and LAMOST spectra, respectively. Stars with available spectra from both ISIS and LAMOST are indicated with a large diamond. The right-hand panels show the histograms and the associated kernel distributions (solid black line) of the  $\delta\text{CN}$  and  $\delta\text{CH}$  residuals. The dashed line represents the Gaussian distribution that best fits the data.

synthetic ones in the spectral window from 4200 to 4400 Å. To compute synthetic templates, we adopted the atmospheric parameters and metallicities derived in Sec. 3 and listed in Table 1. Atomic and molecular line lists were taken from the most recent Kurucz compilation from F. Castelli’s website<sup>5</sup>. Model atmospheres were calculated with the ATLAS9 code (Castelli & Kurucz 2004) using the appropriate temperature and surface gravity for each star. We assumed a microturbulent velocity  $v_t = 2$  km/s for all the stars. Finally, Kurucz’s SYNTHE code (Kurucz 2005) was used to produce model spectra, which were used in a  $\chi^2$  minimisation with the observed spectra to find the absolute carbon abundances,  $A(\text{C})$ . In order to calculate uncertainties from the fit parameters, we iteratively change

<sup>4</sup> To produce histograms and kernel distributions for the *corrected* indices shown in the right-hand panels of Figure 5 we kept measurements from the ISIS data-set only for stars with spectra available in LAMOST.

<sup>5</sup> <https://wwwuser.oats.inaf.it/castelli/>

one parameter by its associated uncertainty and repeat the abundance analysis. Finally, errors introduced by the fitting procedure were estimated by re-fitting a sample of 100 spectra for each star after the introduction of Poissonian noise in the best-fit template.

In the top panel of Figure 6 we show absolute carbon abundances  $A(C)$  plotted against surface gravity. Increasing carbon depletion with rising luminosity is clearly observed in the data. This can be interpreted as a signature of a “deep mixing” process that mixes partially processed (carbon-depleted) material of the stellar interior with the unprocessed material at the surface (e.g. Sweigart & Mengel 1979a; Gratton et al. 2000; Denissenkov & Vandenberg 2003; Martell et al. 2008b). According to Placco et al. (2014), carbon corrections are extremely small ( $\Delta A(C) \leq 0.02$ ) for the majority of the stars analysed here. Larger corrections (spanning values between  $\Delta A(C) = 0.13$ - $0.40$ ) are only expected for the three brightest stars in the sample. We list the index measurements, carbon abundances along with their associated uncertainties for all targets in Table 2. In the same table we also list an evolutionary phase correction for carbon using the results from Placco et al. (2014).

The distribution of the carbon abundances corrected for evolutionary mixing effects,  $A(C)_{\text{cor}}$ , is shown in the middle panel of Figure 6 along with its associated kernel distribution and the Gaussian distribution which best fits data. While most of the stars have  $A(C)_{\text{cor}}$  values around the median value  $A(C)_{\text{cor}} = 6.67$  with a small dispersion, there is a clear outlier (star #9) with  $A(C)_{\text{cor}} = 5.52 \pm 0.07$ . In the bottom panel of Figure 6 we show the spectrum of star #9 around the CH absorption at  $4300\text{\AA}$  as well as the spectrum of a star with similar atmospheric parameters but different C abundance (star #12, with  $A(C)_{\text{cor}} = 6.49 \pm 0.11$ ). The CH band of star #9 looks very weak compared to the stronger absorption observed in star #12. We also show in the same panel the spectra of two fainter objects (star #18 and #20) with nearly identical stellar parameters yet different C content ( $A(C)_{\text{cor}} = 6.75 \pm 0.09$  and  $A(C)_{\text{cor}} = 6.51 \pm 0.06$  for star #18 and #20, respectively). A difference in the CH absorption region is observed also in this case. Visual inspection of the bottom panel of Figure 6 suggests that the intrinsic variations in carbon abundances may be present in the analysed sample. We define C-rich/poor with respect to the median  $A(C)_{\text{cor}}$  value and use different symbols to plot C-rich and C-poor stars in the top panel of Figure 6.

In order to quantitatively assess the presence of an intrinsic spread in carbon, we also repeated our 1-D normal distribution model fit to the corrected  $A(C)$  measurements. This time we find that an intrinsic dispersion of  $\sigma_{0,C} = 0.32 \pm 0.06$ . Given that star #9 is an outlier, we also repeat the fit without it, and find  $\sigma_{0,C} = 0.13 \pm 0.04$ . This point towards some intrinsic dispersion in the C-abundance of GD-1 stars at a  $\sim 3\sigma$  level.

To summarise, we found no statistically significant spreads in the CN and CH indices among the observed RGB stars of GD-1. However, we find evidence for a significant C-abundance spread.

Finally we note that we found no obvious evidence for a spatial segregation of stars with high/low C-abundance. This is supported by a 2-sample Kolmogorov–Smirnov i (KS) test, which suggested that the C-poor and rich populations are drawn from the same distribution in  $\phi_1$  and  $\phi_2 - f(\phi_1)$ . This would indicate that GD-1’s progenitor was fully mixed by the time it started forming the stream. Although a deeper and more homogeneous coverage of the stream would be desirable to investigate this further.

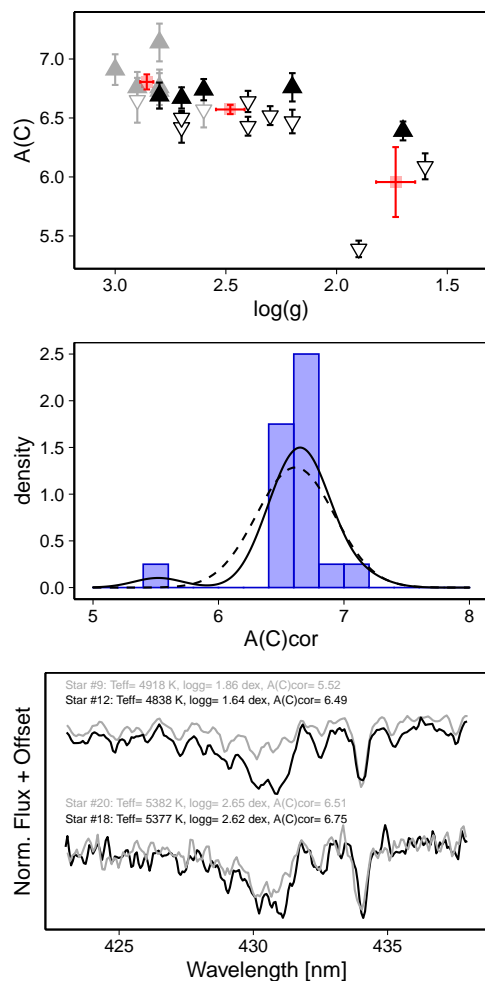


**Figure 6.** The top panels shows the measured absolute carbon abundances  $A(C)$  for all red giants in the sample, with stars identified as C-rich/poor with respect to the median  $A(C)_{\text{cor}}$  value (see text) shown as filled/empty symbols. The three large squares represent the mean and standard error in the luminosity bins:  $\log(g) > 2.75$ ,  $2.0 \leq \log(g) \leq 2.75$ , and  $\log(g) < 2.0$ . There is evidence for some deep mixing: stars in the brightest bin have on average lower carbon abundances than fainter stars. The middle panel shows the histograms and the associated kernel distribution (solid black line) of the absolute carbon abundances corrected for evolutionary effects as in Placco et al. (2014). The dashed line represents the Gaussian distribution that best fits the data. The bottom panel shows spectra of stars with similar atmospheric parameters yet very different C content (see legend). C-rich star spectra are in black, whereas the spectra of C-poor stars are plotted in grey.

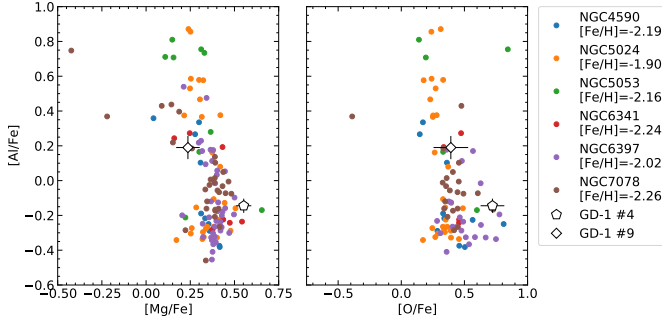
#### 4 APOGEE ABUNDANCES

When we crossmatched our sample of bona fide GD-1 RGB candidates with the DR16 catalogue of APOGEE (Majewski et al. 2017; Ahumada et al. 2020) we found two GD-1 stars in common, stars #4 and #9 (both of these have also blue spectra, see Table 1). Unfortunately APOGEE does not report  $[C/Fe]$  or  $[N/Fe]$  measurements for these stars. However, it does provide measurements for  $[O/Fe]$ ,  $[Al/Fe]$  and  $[Mg/Fe]$  (also known to change from star to star in globular clusters). In Table 3 we summarize the relevant parameters inferred by APOGEE. Overall we found that the stellar parameters and velocities inferred by APOGEE are consistent with our independent measurements described in the previous sections.

The APOGEE abundances of these GD-1 stars show variations

**Table 3.** APOGEE parameters.

ID	$T_{\text{eff}}$ K	$\log g$ dex	$V_{\text{los}}$ km/s	[Fe/H] dex	[O/Fe] dex	[Mg/Fe] dex	[Al/Fe] dex
4	$5089 \pm 135$	$2.39 \pm 0.11$	$98.87 \pm 0.14$	$-2.10 \pm 0.02$	$0.72 \pm 0.09$	$0.55 \pm 0.04$	$-0.14 \pm 0.04$
9	$4938 \pm 160$	$1.55 \pm 0.10$	$-12.30 \pm 0.70$	$-2.27 \pm 0.04$	$0.39 \pm 0.13$	$0.23 \pm 0.07$	$0.19 \pm 0.07$

**Figure 7.** Al, Mg and O abundance from APOGEE DR16. In colour, we show a sample of metal-poor globular cluster stars. In white symbols show GD-1 members #4 and #9. Star #9 is also the one with the lowest C-abundance in our sample.

in [O/Fe], [Mg/Fe] and [Al/Fe] at the  $\sim 2.0\sigma$ ,  $\sim 4.0\sigma$  and  $\sim 4.3\sigma$  levels. In Figure 7 we show the abundances of these GD-1 stars (white symbols) as well as the APOGEE abundances of some Galactic globular clusters with similar metallicity (coloured symbols). This figure shows that the abundance patterns found in GD-1 and Galactic globular clusters of similar metallicity follow a similar behaviour. In particular we note that star #9, i.e. the star with the lowest C-abundance (see previous section), is also the one with the lowest [O/Fe] and [Mg/Fe] and highest [Al/Fe] as expected in globular cluster stars (see Charbonnel 2016; Bastian & Lardo 2018; Gratton et al. 2019).

## 5 DISCUSSION AND CONCLUSION

We demonstrate that a selection method using a combination of optical and (near) UV colours is very successful in identifying RGB members of GD-1, selected according to Gaia eDR3 PM. In this particular case, we have an 81% success rate, which we attribute to the relatively low-metallicity of GD-1 rendering its RGB colour bluer than the bulk of the field population.

We are able to find members associated with off-stream features (*spur* and *blob/cocoon*). We highlight star #23 and #17, which lie  $1.9^\circ$  and  $2.6^\circ$  away from GD-1 respectively. These two stars are the furthest any confirmed GD-1 member has ever been found. Albeit being far from the stream we find no significant velocity offset between the literature GD-1 orbit and these off-stream stars. There are several scenarios for the formation of such features (e.g. Erkal et al. 2016; Bonaca & Hogg 2018; Malhan et al. 2018), these all predict very small velocity offset, which is in agreement with what we observe here.

The study of Galactic and M31 globular clusters have revealed that the more massive clusters show stronger signs of abundance variations than low mass clusters (e.g. Monelli et al. 2013; Schiavon et al. 2013). This is likely a consequence that for the most massive clusters the fraction of stars with anomalous abundance is larger and the magnitude of the abundance variations is stronger (see Milone et al. 2017). The scaling relation between the way the MPs manifest

and the mass of a GC could serve as an independent proxy for stream progenitor masses in the future.

Similarly, it has also been shown that for metal poor GCs, smaller variations in CN are expected as a consequence of the inefficiency to form this molecule (Martell et al. 2008a). Both effects combined, i.e. a low  $\sim 10^4 M_\odot$  mass and low metallicity [Fe/H]  $\sim -2.1$  dex, forecast that any manifestations of the MPs in GD-1 are likely to be subtle.

In our analysis, we find no evidence for a significant spread in CN or CH with the current (large) uncertainties. However, we do find evidence for an intrinsic spread in C-abundances, this detection is significant (at the  $\sim 99\%$  level) even when we remove star #9, which seems to be an outlier in A(C). We observed no evidence for spatial segregation of stars with different C-abundances in our sample, however, future studies with a more homogeneous coverage of the stream should be able to address this more robustly.

The lack of detectable nitrogen variations in stars with intrinsic spread in carbon is not surprising. First, double-metal molecules like CN are particularly difficult to observe at the overall low-metallicity of GD-1 because their absorption strengths rapidly decline with decreasing metallicity and their formation may be partially inhibited even in the presence of substantial [C/Fe] and [N/Fe] differences (e.g. Sneden 1974; Langer et al. 1992). Secondly, their formation depends both on carbon and nitrogen abundances. Deep mixing scenarios predict that mixing efficiency should be high at low-metallicities (e.g. Sweigart & Mengel 1979b). Thus, evolved stars in a low-metallicity cluster like GD-1 will be also depleted in carbon and enhanced in nitrogen because of the dredge-up of CNO processed material. If nitrogen becomes more abundant than carbon as a result of this process, the CN band strength no longer scale monotonically with N abundance and can even decline with rising luminosity (e.g. Smith & Bell 1986; Martell et al. 2008a; Lee & Sneden 2021). As a consequence, in the low-metallicity regime, the CN index has only limited sensitivity to variations in nitrogen (see Fig. 9 of Martell et al. 2008a). On the contrary, absorption features of single-metal molecules like CH do not weaken as much with decreasing metallicity, thus they still trace carbon variations at metallicities [Fe/H]  $< -2.0$ .

We find that two of our confirmed GD-1 members are in the APOGEE DR16 sample. These stars show similar O, Mg and Al abundance variations as the ones found in metal poor Galactic globular clusters in APOGEE. With the GD-1 star with the highest Al abundance also being the one with the lowest C, O and Mg abundances. This suggests that GD-1 also manifests the multiple stellar population phenomenon characteristic of more massive, undissolved globular clusters.

If the MPs signal is confirmed, it would make GD-1 the lowest mass GC in the [Fe/H]  $< -2.0$  regime to have displayed the phenomena. This has implications both to the different scenarios for MPs and to the origin of GD-1. In some scenarios (e.g. Elmegreen 2017; Gieles et al. 2018), the formation of MPs is closely tied to a high gas density/pressure environment, thus not allowing for such a low initial mass system as GD-1 to have been formed in those conditions. One could argue that GD-1's initial mass – as inferred by Webb & Bovy (2019) or de Boer et al. (2020) – depends on the mass-loss while orbiting the Galaxy. It is possible that GD-1 belonged to an accreted host galaxy, and had some of its mass striped while in the original host. In this case, it could place it in an initial mass range compatible with Galactic GCs. To confirm the accreted scenario, observing the remnant of the host would be crucial to date the time of accretion and host mass, allowing for stronger constraints on GD-1's initial mass.



Even though Gaia helped immensely the target selection for streams, looking for additional evidence of light element spreads and for the possible host galaxy that brought GD-1 into the Galaxy will be a task for future large high multiplexing spectroscopic surveys. In the near-future, we expect WEAVE (Dalton et al. 2016), to observe all of GD-1's RGB members in high/medium resolution, and provide insight into MPs in this stream and their spatial distribution. Using the same target selection technique used here, we expect to target up to 100 GD-1 members per linear degree in WEAVE's low-resolution halo survey. This work is the first study of the MPs phenomena for a completely dissolved GC and we show the potential for using streams to open up a new region of parameters space, not available in the local Universe population of GCs.

We also point out, that for more metal rich streams, where the CN band is stronger, may be promising targets since their RGBs will split into multiple components in  $C_{\text{ugr}}$  space, allowing for the study of the distribution of different populations along the stream using photometry alone.

Finally, we would like to mention that our findings support the idea that the small number (few percent) of halo field stars known to display chemical patterns characteristic of globular cluster stars, originated from disrupted/disrupting globular cluster (e.g. Martell et al. 2016; Schiavon et al. 2017; Koch et al. 2019; Hanke et al. 2020; Horta et al. 2021).

## ACKNOWLEDGEMENTS

The authors would like to thank Nate Bastian, Mark Gieles, Amina Helmi, Jeremy Webb, and Ricardo Schiavon for the comments and discussions during the early stages of this work.

EB acknowledges support from a Vici grant from the Netherlands Organization for Scientific Research (NWO).

Support for this work was provided by NASA through Hubble Fellowship grant HST-HF2-51387.001-A awarded by the Space Telescope Science Institute, which is operated by the Association of Universities for Research in Astronomy, Inc., for NASA, under contract NAS5-26555.

CL acknowledges funding from Ministero dell'Università e della Ricerca through the Programme "Rita Levi Montalcini" (grant PGR18YRML1).

The William Herschel Telescope and its service programme are operated on the island of La Palma by the Isaac Newton Group of Telescopes in the Spanish Observatorio del Roque de los Muchachos of the Instituto de Astrofísica de Canarias.

This work has made use of data from the European Space Agency (ESA) mission *Gaia* (<https://www.cosmos.esa.int/gaia>), processed by the *Gaia* Data Processing and Analysis Consortium (DPAC, <https://www.cosmos.esa.int/web/gaia/dpac/consortium>). Funding for the DPAC has been provided by national institutions, in particular the institutions participating in the *Gaia* Multilateral Agreement.

Funding for SDSS-III has been provided by the Alfred P. Sloan Foundation, the Participating Institutions, the National Science Foundation, and the U.S. Department of Energy Office of Science. The SDSS-III web site is <http://www.sdss3.org/>.

SDSS-III is managed by the Astrophysical Research Consortium for the Participating Institutions of the SDSS-III Collaboration including the University of Arizona, the Brazilian Participation Group, Brookhaven National Laboratory, Carnegie Mellon University, University of Florida, the French Participation Group, the German Participation Group, Harvard University, the Instituto de

Astrofísica de Canarias, the Michigan State/Notre Dame/JINA Participation Group, Johns Hopkins University, Lawrence Berkeley National Laboratory, Max Planck Institute for Astrophysics, Max Planck Institute for Extraterrestrial Physics, New Mexico State University, New York University, Ohio State University, Pennsylvania State University, University of Portsmouth, Princeton University, the Spanish Participation Group, University of Tokyo, University of Utah, Vanderbilt University, University of Virginia, University of Washington, and Yale University.

Guoshoujing Telescope (the Large Sky Area Multi-Object Fiber Spectroscopic Telescope LAMOST) is a National Major Scientific Project built by the Chinese Academy of Sciences. Funding for the project has been provided by the National Development and Reform Commission. LAMOST is operated and managed by the National Astronomical Observatories, Chinese Academy of Sciences.

The following software packages were used in this publication: *Astropy* (Astropy Collaboration et al. 2013; Price-Whelan et al. 2018), *gala* (Price-Whelan 2017), *IPython* (Pérez & Granger 2007), *matplotlib* (Hunter 2007), *numpy* (Walt et al. 2011), *scipy* (Jones et al. 01) *vaex* (Breddels & Veljanoski 2018)

## DATA AVAILABILITY

The data underlying this article will be shared on reasonable request to the corresponding author.

## REFERENCES

- Ahumada R., et al., 2020, *ApJS*, 249, 3
- Astropy Collaboration et al., 2013, *A&A*, 558, A33
- Balbinot E., et al., 2016, *ApJ*, 820, 58
- Bastian N., Lardo C., 2018, *ARA&A*, 56, 83
- Bernard E. J., et al., 2016, *MNRAS*, 463, 1759
- Bonaca A., Hogg D. W., 2018, preprint
- Bragaglia A., Carretta E., D'Orazi V., Sollima A., Donati P., Gratton R. G., Lucatello S., 2017, *A&A*, 607, A44
- Breddels M. A., Veljanoski J., 2018, *A&A*, 618, A13
- Bressan A., Marigo P., Girardi L., Salasnich B., Dal Cero C., Rubele S., Nanni A., 2012, *MNRAS*, 427, 127
- Cardelli J. A., Clayton G. C., Mathis J. S., 1989, *ApJ*, 345, 245
- Carrera R., Martínez-Vázquez C. E., 2013, *A&A*, 560, A5
- Castelli F., Kurucz R. L., 2004, *A&A*, 419, 725
- Chambers K. C., et al., 2016, preprint
- Charbonnel C., 2016, in *EAS Publications Series*. pp 177–226, doi:10.1051/eas/1680006
- D'Ercole A., D'Antona F., Vesperini E., 2016, *MNRAS*, 461, 4088
- Dallessandro E., et al., 2019, *ApJ*, 884, L24
- Dalton G., et al., 2016, *SPIE*, 9908
- Denissenkov P. A., VandenBerg D. A., 2003, *ApJ*, 593, 509
- Eisenstein D. J., et al., 2011, *AJ*, 142, 72
- Elmegreen B. G., 2017, *ApJ*, 836, 80
- Erkal D., Sanders J. L., Belokurov V., 2016, *MNRAS*, 461, 1590
- Foreman-Mackey D., Hogg D. W., Lang D., Goodman J., 2013, *PASP*, 125, 306
- Gaia Collaboration Brown A. G. A., Vallenari A., Prusti T., de Bruijne J. H. J., Babusiaux C., Bailer-Jones C. A. L., 2018, preprint, 616, A1
- Gaia Collaboration et al., 2020, *VizieR Online Data Catalog*, pp J/A+A/649/A6
- Gieles M., et al., 2018, *MNRAS*, 478, 2461
- Gieles M., Erkal D., Antonini F., Balbinot E., Peñarrubia J., 2021, *Nat Ast*
- Gillessen S., Eisenhauer F., Trippe S., Alexander T., Genzel R., Martins F., Ott T., 2009, *ApJ*, 692, 1075
- Gratton R. G., Sneden C., Carretta E., Bragaglia A., 2000, *A&A*, 354, 169

- Gratton R., Bragaglia A., Carretta E., D'Orazi V., Lucatello S., Sollima A., 2019, *A&ARv*, 27, 8
- Grillmair C. J., Dionatos O., 2006, *ApJ*, 643, L17
- Hanke M., Koch A., Prudil Z., Grebel E. K., Bastian U., 2020, *A&A*, 637, A98
- Hénault-Brunet V., Gieles M., Agertz O., Read J. I., 2015, *MNRAS*, 450, 1164
- Hollyhead K., et al., 2017, *MNRAS*, 465, L39
- Hollyhead K., et al., 2018, *MNRAS*, 476, 114
- Hollyhead K., et al., 2019, *MNRAS*, 484, 4718
- Horta D., et al., 2021, *MNRAS*, 500, 5462
- Hunter J. D., 2007, *Computing in Science and Engineering*, 9, 90
- Husser T. O., Wende-von Berg S., Dreizler S., Homeier D., Reiners A., Barman T., Hauschildt P. H., 2013, *A&A*, 553, A6
- Ibata R. A., Malhan K., Martin N. F., 2019, *ApJ*, 872, 152
- Johnson C. I., Caldwell N., Michael Rich R., Mateo M., Bailey J. I., 2019, *MNRAS*, 485, 4311
- Jones E., Oliphant T., Peterson P., et al., 2001–, SciPy: Open source scientific tools for Python, <http://www.scipy.org/>
- Kayser A., Hilker M., Grebel E. K., Willemsen P. G., 2008, *A&A*, 486, 437
- Koch A., Grebel E. K., Martell S. L., 2019, *A&A*, 625, A75
- Koposov S. E., Rix H.-W., Hogg D. W., 2010, *ApJ*, 712, 260
- Küpper A. H. W., Balbinot E., Bonaca A., Johnston K. V., Hogg D. W., Kroupa P., Santiago B. X., 2015, *ApJ*, 803, 80
- Kurucz R. L., 2005, *Memorie della Societa Astronomica Italiana Supplementi*, 8, 14
- Kuzma P. B., Da Costa G. S., Mackey A. D., 2018, *MNRAS*, 473, 2881
- Langer G. E., Suntzeff N. B., Kraft R. P., 1992, *PASP*, 104, 523
- Lardo C., Bellazzini M., Pancino E., Carretta E., Bragaglia A., Dalessandro E., 2011a, *A&A*, 525, A114
- Lardo C., Bellazzini M., Pancino E., Carretta E., Bragaglia A., Dalessandro E., 2011b, *A&A*, 525, A114
- Lardo C., et al., 2013, *MNRAS*, 433, 1941
- Larsen S. S., Baumgardt H., Bastian N., Brodie J. P., Grundahl F., Strader J., 2015, *ApJ*, 804, 71
- Lee J.-W., Sneden C., 2021, *ApJ*, 909, 167
- Li G.-W., Yanny B., Wu Y., 2018, *ApJ*, 869, 122
- MacLean B. T., De Silva G. M., Lattanzio J., 2015, *MNRAS*, 446, 3556
- Majewski S. R., et al., 2017, *AJ*, 154, 94
- Malhan K., Ibata R. A., Martin N. F., 2018, preprint
- Marino A. F., Villanova S., Piotto G., Milone A. P., Momany Y., Bedin L. R., Medling A. M., 2008, *A&A*, 490, 625
- Martell S. L., Smith G. H., 2009, *PASP*, 121, 577
- Martell S. L., Smith G. H., Briley M. M., 2008a, *PASP*, 120, 7
- Martell S. L., Smith G. H., Briley M. M., 2008b, *AJ*, 136, 2522
- Martell S. L., et al., 2016, *ApJ*, 825, 146
- Martocchia S., et al., 2021, *MNRAS*, 505, 5389
- Massari D., Koppelman H. H., Helmi A., 2019, *A&A*, 630, L4
- Milone A. P., et al., 2017, *MNRAS*, 464, 3636
- Monelli M., et al., 2013, *MNRAS*, 431, 2126
- Norris J., Freeman K. C., 1979, *ApJ*, 230, L179
- Norris J., Cottrell P. L., Freeman K. C., Da Costa G. S., 1981, *ApJ*, 244, 205
- Odenkirchen M., et al., 2001, *ApJ*, 548, L165
- Pancino E., Rejkuba M., Zoccali M., Carrera R., 2010, *A&A*, 524, A44
- Pérez F., Granger B. E., 2007, *Computing in Science and Engineering*, 9, 21
- Placco V. M., Frebel A., Beers T. C., Stancliffe R. J., 2014, *ApJ*, 797, 21
- Price-Whelan A. M., 2017, *The Journal of Open Source Software*, 2, 388
- Price-Whelan A. M., Bonaca A., 2018, *ApJ*, 863, L20
- Price-Whelan A. M., et al., 2018, *AJ*, 156, 123
- Salinas R., Strader J., 2015, *ApJ*, 809, 169
- Schiavon R. P., Caldwell N., Conroy C., Graves G. J., Strader J., MacArthur L. A., Courteau S., Harding P., 2013, *ApJ*, 776, L7
- Schiavon R. P., et al., 2017, *MNRAS*, 465, 501
- Schlegel D. J., Finkbeiner D. P., Davis M., 1998, *ApJ*, 500, 525
- Schönrich R., Binney J., Dehnen W., 2010, *MNRAS*, 403, 1829
- Shipp N., Drlica-Wagner A., Balbinot E., DES Collaboration 2018, in *American Astronomical Society Meeting Abstracts #231*. p. 212.05
- Skrutskie M. F., et al., 2006, *AJ*, 131, 1163
- Smith G. H., Bell R. A., 1986, *AJ*, 91, 1121
- Sneden C., 1974, *ApJ*, 189, 493
- Sollima A., 2020, *MNRAS*, 495, 2222
- Speagle et al. 2021, submitted
- Sweigart A. V., Mengel J. G., 1979a, *ApJ*, 229, 624
- Sweigart A. V., Mengel J. G., 1979b, *ApJ*, 229, 624
- Vásquez S., Zoccali M., Hill V., Gonzalez O. A., Saviane I., Rejkuba M., Battaglia G., 2015, *A&A*, 580, A121
- Venables W. N., Ripley B. D., 2002, *Modern Applied Statistics with S*, fourth edn. Springer, New York, <http://www.stats.ox.ac.uk/pub/MASS4>
- Vollmann K., Eversberg T., 2006, *Astronomische Nachrichten*, 327, 862
- Walt S. v. d., Colbert S. C., Varoquaux G., 2011, *Computing in Science and Engg.*, 13, 22
- Webb J. J., Bovy J., 2019, *Monthly Notices of the Royal Astronomical Society*, 485, 5929–5938
- de Boer T. J. L., Belokurov V., Koposov S. E., Ferrarese L., Erkal D., Côté P., Navarro J. F., 2018, *MNRAS*, 477, 1893
- de Boer T. J. L., Erkal D., Gieles M., 2020, *MNRAS*, 494, 5315

This paper has been typeset from a  $\text{\LaTeX}$  file prepared by the author.